

Results from Loads and Aeroelastic Analyses of a High Altitude, Long Endurance, Solar Electric Aircraft

(Received: June 26, 2021. Revised: Dec 6, 2021. Accepted: Dec 28, 2021)

ARNE VOSS¹
VEGA HANDOJO¹
STEFFEN NIEMANN²
CHRISTIAN WEISER³

Abstract

This work presents the results of comprehensive loads and aeroelastic analyses for the design of the high altitude, long endurance, solar electric aircraft HAP. To ensure a sophisticated design, a large number of maneuver, gust, gyroscopic and landing loads cases are considered. The structural sizing results in a total primary structural mass of 38.4 kg, which is very low considering the wing span of ≈ 28.0 m. The extreme light-weight construction (wing loading ≈ 4.0 kg/m²) leads to a highly flexible aircraft, making aeroelastic analyses mandatory. Results of static and dynamic aeroelastic analyses are presented, showing that the resulting design is plausible from an aeroelastic point of view.

1. Motivation and Introduction

The High Altitude Platform (HAP) is a very light weight, high altitude and long endurance aircraft (HALE) designed to stay airborne and hold position for several days at an altitude between FL450 and FL800. Carrying optical measurement equipment, this allows scientists to make observations of the earth continuously for a long period of time. This is an advantage compared to satellites, which typically pass the same spot only every couple of days and fly much higher, leading e.g. to a lower optical resolution. The ability to start and land allows to re-configure and re-locate the aircraft for new and different missions. In addition, purchase and operation costs of an aircraft are expected to be much lower compared to those of a satellite, including the infrastructure (airfield vs. spaceport). An illustration of the HAP configuration, currently under development at the DLR, is shown in Figure 1. The idea is to create a flight vehicle that flies very slow ($V_{EAS} = 9.0 \dots 11.0$ m/s) but is highly efficient in terms of propulsion and aerodynamic performance and is powered by solar electric energy. This requires a design which offers large areas for the installation of solar panels and is very light weight at the same time. During the night, the altitude is decreased and batteries are used, which are then re-charged during daytime while the aircraft re-gains altitude. Similar configurations, which are currently under development in the industry, are the Airbus Zephyr [1, 2] (formerly developed by QinetiQ) or the Phasa-35 [3] by BAE Systems. Other comparable aircraft with and without a tailplane are the Solar Impulse [4] or the NASA Helios prototype [5]. The first two examples are planned for commercial use while the latter have a more scientific background.

This paper is the second in a series of publications. In the first publication [6], the authors focused on:

- a literature study on the aeroelastic behavior and modeling of other HALE configurations

¹ Loads and Aeroelasticity Engineer, DLR - German Aerospace Center, Institute of Aeroelasticity, Göttingen, Germany, arne.voss@dlr.de, vega.handojo@dlr.de

² Structural Engineer, DLR - German Aerospace Center, Institute of Composite Structures and Adaptive Systems, Braunschweig, Germany, steffen.niemann@dlr.de

³ Flight Control Engineer, DLR - German Aerospace Center, Institute of System Dynamics and Control, Weßling, Germany, christian.weiser@dlr.de

- the modeling strategies and the selection of appropriate methods and tools to capture the anticipated aeroelastic effects
- a presentation of the resulting models
- the structural sizing process, including first mass estimates and the structural dynamic properties

During the progress of the project, the aircraft design has evolved and matured (from version HAP-O2 presented in [6]) to the current design (version HAP-O6). On the one hand, more analyses have been performed, leading to a better knowledge and understanding of the configurations. On the other hand, the underlying data has improved, e.g. estimates of system masses have been replaced by the actual masses of the real components. Finally, the design became more detailed from a construction point of view (detailed CAD design of parts, drawings, manufacturing of prototypes, etc.), leading to more reliable mass and stiffness properties. Minor changes in the geometry were introduced, for example the dihedral angle and taper ratio of the outer wing changed, the airfoils were modified, etc., and the project passed a preliminary design review and is now heading towards the critical design review. At this stage, the configuration is not yet fixed, but a large number of analyses have been performed and the authors believe that the results presented in this publication are representative for the final configuration. This paper covers a large number of topics, listed and structured as follows.

Section 2. presents

- a short repetition of the aeroelastic modeling
- the structural dynamic properties and
- a summary of the flight controller design.

Section 3. focuses on the loads analysis, including

- maneuver loads,
- closed-loop 1-cos gust loads,
- propulsion, engine torque and gyroscopic loads from the propellers,
- landing loads and
- structural sizing.

Section 4. presents aeroelastic analyses, including

- jig and flight shapes,
- control surface effectiveness,
- longitudinal stability,
- a flutter check and
- the interaction of elastic modes with flight mechanics.

A summary and an outlook on further activities planned on the road towards the first flight is given in section 5..

2. Aeroelastic Modeling

A detailed description of the aeroelastic models is given in Voß et al. [6]. Because there have been no general changes, in the following, the structural, mass and aerodynamic modeling are describe briefly as a short repetition and for completeness. The flight controller, however, has evolved and matured significantly with respect to [6].

2.1 Structural Modeling

Because of the slender, beam-like structure of the configuration, mainly beam and bar elements are used. The element stiffness and material characteristics



Figure 1: Early artist impression of the High Altitude Platform (HAP).

are provided by the DLR Institute of Composite Structures and Adaptive Systems and are converted to a MSC.Nastran model using a combination of the parameterized model generator ModGen [7] and Excel. The resulting beam model is shown in Figure 2a and consists of 326 GRID points, which are shown in Figure 2b. The stiffness properties are then extracted from MSC.Nastran (stiffness matrix \mathbf{K}_{gg}) to be used in the DLR in-house loads and aeroelastic analysis software Loads Kernel [8].

2.2 Mass Modeling

Structural masses are derived from the material thicknesses and densities, and are complemented by the system masses, which are provided by the DLR Institute of Flight Systems. All masses are attached as condensed masses (CONM2) to the closest structural grid points. Note that the structural and mass models are treated separately because some structural members (e.g. secondary structure) are not included in the beam model but should be accounted for in the mass model. Currently, two mass configurations (M1 and M2) are considered for the loads analyses, one equipped with all solar panels and one with a reduced number of solar panels, which will be used for shorter flights at low altitudes, e.g. during flight testing. The corresponding mass distribution is shown in Figure 2c and only for M1, because the differences are small. The volume of the yellow spheres is proportional to the mass they represent and the large, transparent sphere indicates the center of gravity. All planned payloads weight close to 5 kg and are mounted at the same location in the forward fuselage. Because the remaining equipment is fixed and no mass change due to fuel combustion occurs, two mass configurations are sufficient. Depending on the weight of the additional measurement equipment, the flight test configuration might be considered as an additional mass case once the actual measurement systems are known. Like the stiffness properties, the mass properties are extracted from MSC.Nastran (mass matrices \mathbf{M}_{gg}) as well.

2.3 Structural Dynamics

The eigenforms and -frequencies characterize the structural dynamic behavior of an aircraft and are important for further aeroelastic analyses. Figure 3 shows the first four flexible mode shapes, calculated for the unconstrained aircraft in vacuum. The frequency of the first wing bending, shown in Figure 3a, has increased slightly from 0.8 Hz to 1.28 Hz compared to [6], which can be explained by a more realistic distribution of the battery masses, which have shifted towards the inner wing. The frequency of the first in-plane wing bending, shown in Figure 3b, coincides with the first wing bending, which can be explained by the tube-type spar, which has the same stiffness properties in all directions.

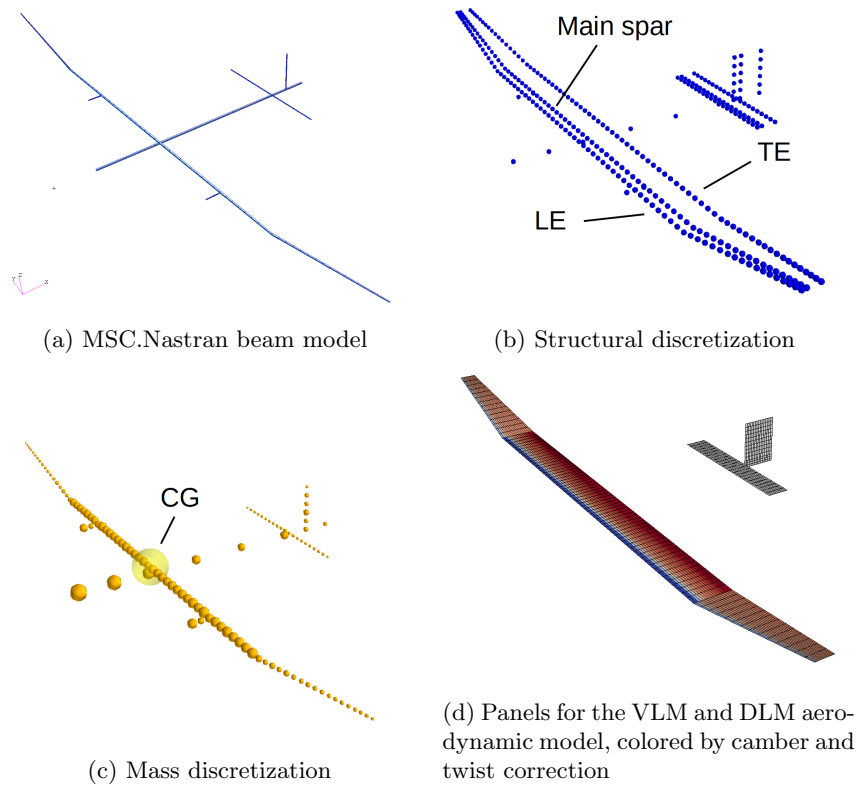


Figure 2: Discretization of the HAP-O6 aeroelastic models.

However, the first wing bending also has some in-plane components and vice versa, so the two modes are not separated clearly and typically occur in combination. This behavior will change as soon as for example a leading and trailing edge are defined structurally. The third flexible mode, shown in Figure 3c, is a combination of in-plane fuselage bending plus antisymmetric wing bending and the fourth mode shape, shown in Figure 3d, is the first antisymmetric wing bending plus some fuselage torsion. The four modes presented above are intended as an example, for the aeroelastic modeling up to 50 modes are included, which corresponds to frequencies of up to $f \approx 45 \text{ Hz}$.

2.4 Aerodynamic Modeling

The design maneuvering speed is 9.1 m/s EAS with a stall speed at 6.5 m/s EAS and a maximum cruise speed of 11.0 m/s EAS. The altitude ranges from sea level up to 25.0 km, as the aircraft is supposed to fly most of the time above the regular air traffic, except for climb and descent phases. The airfoils of the wing (MH169 airfoil family) are specially designed by the DLR Institute of Aerodynamics and Flow Technology to deliver optimal performance under these operational conditions. Both Reynolds (typical range $Re = 150,000 \dots 1,000,000$) and Mach numbers (up to $Ma = 0.3$) are moderate and well within the subsonic regime. Thus, aerodynamic panel methods such as the steady vortex lattice method (VLM) and the unsteady doublet lattice method (DLM) yield an acceptable representation of the lifting surfaces. All lifting surfaces (wing, horizontal and vertical tail) are modeled, resulting in an aerodynamic panel mesh shown in Figure 2d. The aerodynamic panels are corrected for airfoil camber, geometrical pre-twist along the wing-span, and an angle of incidence. A full documentation of the implementation, the equations involved as well as a validation of the resulting pressure distributions is given in a technical report by Voß [9].

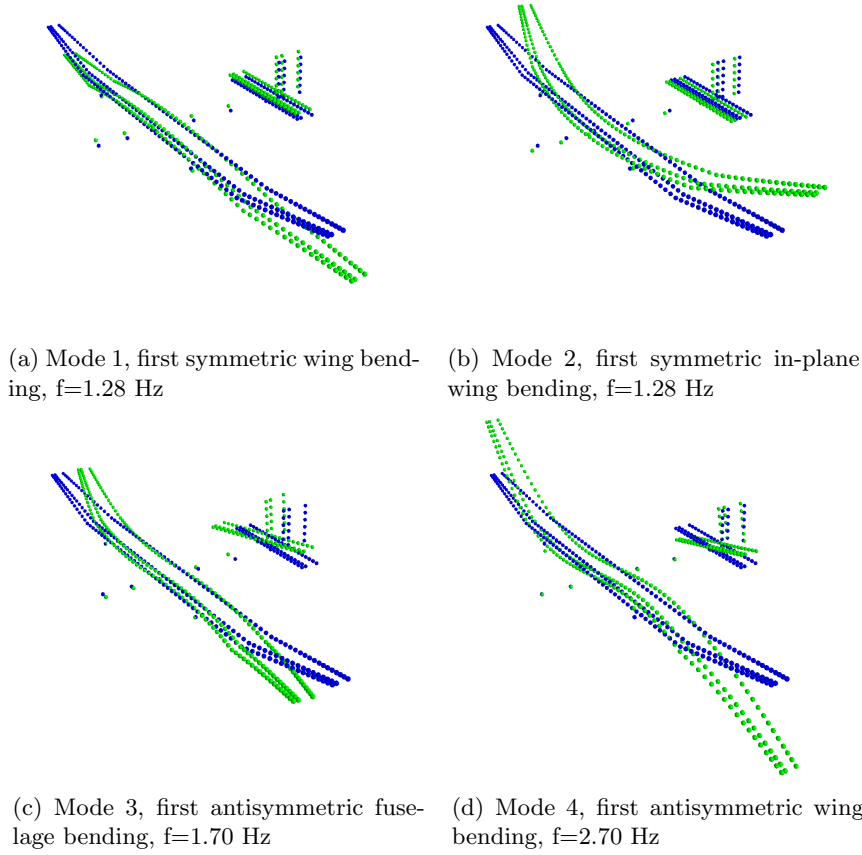


Figure 3: First four flexible mode shapes, M1.

2.5 Flight Mechanical Interaction

Flight mechanical aspects of the free-flying aircraft are included in the equation of motion following Waszak, Schmidt and Buttrill [10, 11, 12]. The motion of the aircraft is divided into a rigid and a flexible part. For the rigid body motion, the aircraft is considered as a point mass with inertia matrices \mathbf{M}_b and \mathbf{I}_b , where the components of the inertia tensor \mathbf{I}_b are calculated with respect to the body axes 'b'. Its origin is located at the center of gravity. All external forces and moments \mathbf{p}_g^{ext} , including the aerodynamics, landing gear and propulsion loads, are gathered at the same point. The non-linear equations of motion given by

$$\dot{\mathbf{v}}_b = \mathbf{M}_b^{-1} \cdot \mathbf{p}_b^{\text{ext, forces}} + \mathbf{v}_b \times \boldsymbol{\omega}_b + \dot{\mathbf{v}}_b^{\text{grav}} \quad (1)$$

and

$$\dot{\boldsymbol{\omega}}_b = \mathbf{I}_b^{-1} \cdot (\mathbf{p}_b^{\text{ext, moments}} - \boldsymbol{\omega}_b \times (\mathbf{I}_b \cdot \boldsymbol{\omega}_b)) \quad (2)$$

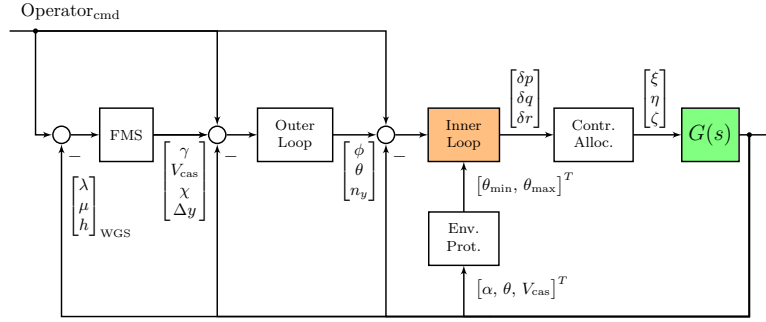
yield the translational and rotational accelerations $\dot{\boldsymbol{\omega}}_b$ and $\dot{\mathbf{v}}_b$ of the aircraft body frame. In addition to the rigid body motion of the aircraft, linear structural dynamics are incorporated by

$$\mathbf{M}_{ff} \ddot{\mathbf{u}}_f + \mathbf{D}_{ff} \dot{\mathbf{u}}_f + \mathbf{K}_{ff} \mathbf{u}_f = \mathbf{p}_f^{\text{ext}} \quad (3)$$

Here, generalized external forces $\mathbf{p}_f^{\text{ext}}$ interact with linear elastic deflections \mathbf{u}_f , velocities $\dot{\mathbf{u}}_f$ and accelerations $\ddot{\mathbf{u}}_f$. The matrices \mathbf{M}_{ff} , \mathbf{D}_{ff} and \mathbf{K}_{ff} refer to the generalized mass, damping, and stiffness matrices.

A publication dedicated to the flight mechanical analyses is presented by Hasan et al. [13]. A main difference between the flight mechanical and the aeroelastic model is the aerodynamic approach and the way elasticity is included. The aerodynamic data for flight mechanical simulations is typically more detailed and includes more aerodynamic effects (e.g. drag, roll-yaw-coupling, etc.),

Figure 4: Architecture of the proposed flight control system.



but is given in terms of global coefficients while the VLM and DLM used in this work calculate a pressure distribution, which is a pre-requisite to natively include elastic deformations. Summing up, this work includes flight mechanical effects but does not replace a dedicated flight mechanical analysis.

2.6 Flight Control System

The aircraft possesses a flight control system, which is prepared by the DLR Institute of System Dynamics and Control. The selected flight control system architecture is depicted in Figure 4. From left to right (or outer to inner), the command signals are

- Flight Management System (FMS): World Geodetic System (WGS) longitude, latitude and altitude $[\lambda \ \mu \ h]^T$.
- Outer loop: flight path angle, calibrated airspeed, ground track angle, cross track error $[\gamma \ V_{\text{cas}} \ \chi \ \Delta y]^T$.
- Inner loop: pitch & bank attitude, lateral acceleration $[\Phi \ \Theta \ n_y]^T$.
- Control allocation: moment demands in roll, pitch and yaw.

The resulting outputs to the controlled plant, namely the aeroelastic aircraft, are the aileron, elevator and rudder deflections ($[\xi \ \eta \ \zeta]^T$). Moreover, the engine thrust is directly commanded by the outer loop (connection is not depicted in Figure 4). The feedback signals are not displayed separately, as they correspond to the command signals for all cases except the inner loop, where feedback of the Euler rates is evaluated in addition to the control variables. In order to offer suitable modes for autonomous flight during nominal operation, as well as lower level modes for testing, this cascaded flight control structure was selected. For the closed-loop analyses in section 3, the outer loop and the FMS are neglected, as they are designed for low frequency guidance tasks (bandwidth < 0.1 Hz). This is less than 10% of the first flexible mode's frequency (compare to Figure 3a), which backs the assumption that the outer loop is not relevant for the loads analysis. This section will thus focus on the development of the inner loop control laws for the HAP configuration, highlighted in orange in Figure 4.

The inner loop control design is divided into longitudinal and lateral dynamics, as both can be regarded as sufficiently decoupled. The design process for each axis follows a standardized design process similar to [14, 15] with the three steps:

- Definition of requirements
- Selection of a suitable control architecture and controller synthesis
- Verification of the resulting controller and closed-loop system

The requirements used for the control design emerge only partially from higher level project specifications, but mostly they are derived from analyses as performed within this paper and previously presented [6] work. In addition, norms

| Req. | Name | Rationale | MoC |
|------|---------------------------------|--|----------------------------|
| 1 | nominal stability for all modes | $\text{Re}(\lambda_i) < 0$ | Eigenvalues of closed-loop |
| 2 | gain & phase margins | 6dB/45deg: $f < f_{\text{flex}}$ 8dB/60deg: $f > f_{\text{flex}}$ | Nichols diamonds |
| 3 | short period damping | $\zeta > 0.6$ | Eigenvalues of closed-loop |

Table 1: Selected Inner Loop Requirements.

and guidelines for control design and handling qualities [16, 17], as well as literature related to control design for similar projects [14], is assessed for a derivation of requirements. The most important stability and robustness requirements are listed in Table 1 and some details on the selection process of these requirements is given in the following comments:

- 1 For stability of the closed-loop system.
- 2 The conventional 6 dB, 45 deg margins are extended to 8 dB, 60 deg for frequencies starting at the frequency of the first flexible aircraft mode ($\equiv f_{\text{sp}}$).
- 3 Sufficient damping of the short period mode [17].

For tuning of the control laws, the aeroelastic model described in sections 2.1 to 2.4 is used. States, which do not influence the aircraft motion in the symmetric (for longitudinal control design) / asymmetric (lateral control) plane, are truncated. This reduces the model complexity and computational cost for control synthesis. The reduced models include the rigid body states angle of attack, pitch rate, pitch attitude and airspeed $[\alpha, q, \Theta, V]^T$, as well as ten structural modes (compare with section 2.3 and Figure 3) in the longitudinal case.

In order to link the possibilities of manual and automated control and provide a suitable interface for the autopilot, a Rate Command Attitude Hold (RCAH) architecture was selected. The RCAH control law allows the pilot to command rate commands whereas the autopilot feeds an attitude command. For synthesis of the control laws, the components of the RCAH architecture are tuned in an optimization process, which considers simplified actuator and sensor dynamics of PT1 form attached to the previously described aircraft model. The used optimization constraints correspond to the stability requirements in Table 1 and some additional performance requirements.

For the attitude hold part of the inner loop control law, the pitch error is defined as the difference between reference pitch attitude and actual pitch attitude

$$e_{\Theta} = \Theta_{\text{ref}} - \Theta_{\text{meas}}. \quad (4)$$

The attitude hold control law can thus be formulated as a parameter dependent proportional integral derivative (PID) controller of the form

$$\eta(V, h) = K_P(V, h)e_{\Theta} + K_I(V, h)e_{\Theta} + K_D(V, h)\dot{\Theta}_{\text{meas}} \quad (5)$$

where $K_i(\rho)$ are the controller gains dependent of a parameter vector ρ . The gain-scheduling is inherently regarded in the optimization with a basis function of

$$K_i(V_{\text{eas}}, h) = k_{0,i} + k_{1,i}V_{\text{eas}} + k_{2,i}h + k_{3,i}V_{\text{eas}}h \quad (6)$$

for each gain. Note, that the parameter vector ρ equals $[V_{\text{eas}}, h]^T$ in this case.

Specific details on the proposed RCAH control structure, especially the rate only part for pilot command, as well as the design results for longitudinal and lateral inner loop control are discussed in [18]. The synthesis process used a well proven optimization process for scheduled flight control laws [19, 20].

For verification of the control laws, besides the assessment of design goals in the frequency domain [18], a set of non-linear simulations is performed in order

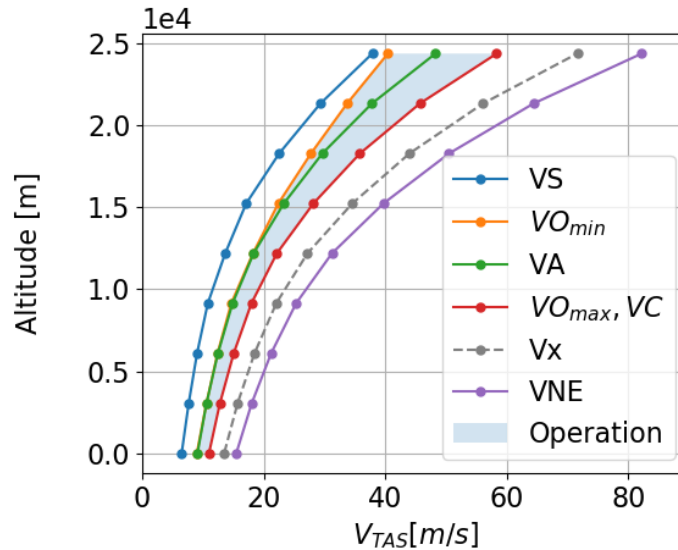


Figure 5: Proposed design speeds.

to check the stability and robustness of the closed-loop system. Non-linear simulation based verification procedures include the 1-cos gust simulations for a set of applicable gusts over the flight envelope, as well as maneuver simulations with different command cases.

3. Loads Analysis

3.1 Load Cases

The aircraft is sized by maneuver, gust, landing and engine loads. For the selection of load cases, mainly CS-23 Amendment 3 [21] is taken as a guideline. Other specifications like CS-22 or CS-VLA might match better judged by the size of the aircraft but the selected methods and tools harmonize better with CS-23 or even CS-25. Note that most prescribed parameters such as load factors, speeds, etc. are too high and not directly applicable to the HAP configuration. These parameters are modified based on engineering judgment and estimates, which will be refined and/or confirmed by more sophisticated requirements and results from flight mechanical analyses in the following phases of the aircraft development.

The velocities and altitudes considered for the aircraft design are shown in Figure 5 and each dot marks one operation point. The airspeeds considered in loads analyses are primarily VS, VA, VC and VNE. Velocities VO_{\min} and VO_{\max} indicate the nominal operational range. Velocity Vx is used as an additional sample point in the subsequent aeroelastic analyses (see section 4.) to bridge the gap between VC and VNE due of the comparatively large difference in dynamic pressure q_{∞} .

An overview of the types and numbers of load cases is given in Table 2. For maneuver loads, 15 different vertical maneuvers, 24 different roll maneuvers and six different yaw maneuvers are considered. Application to the different altitudes, flight speeds and mass configurations leads to a total number of 1260 maneuver load cases. Note that not all maneuvers are performed at each operational point, for example there is no pull-up at VS. Discrete gusts of 1-cos type are simulated with seven different gust gradient ranging from $H = 5 \dots 61 \text{ m}$. The aircraft encounters both positive and negative gusts in vertical and horizontal direction as well as orthogonal to the outer wings, leading to a total number of 2016 gust load cases. Because of the variety in flight speeds and gust gradients, the simulated time ranges from 1 to 20 seconds. Because the time integration is computationally expensive, one gust encounter takes several

| Description | Number |
|-----------------------------|--------|
| Operational points | |
| Altitudes | 9 |
| Speeds | 4 |
| Mass configurations | 2 |
| Vertical maneuvers | 15 |
| Roll maneuvers | 24 |
| Yaw maneuvers | 6 |
| Total Maneuver load cases | 1260 |
| Gust gradients | 7 |
| Gust directions | 8 |
| Total gust load cases | 2016 |
| Approach speeds | 2 |
| Sink rates | 2 |
| Total landing load cases | 4 |
| Engine operational points | 6 |
| Total propulsion load cases | 54 |

Table 2: Overview of type and number of load cases considered.

minutes of computational time and all gust load cases and take ≈ 22 hours on 48 CPUs. For comparison, all maneuver loads are calculated within ≤ 10 minutes. The maneuver and gust load cases are complemented by four different landing scenarios, where the landing impact from the landing skids is simulated. In addition, there are 54 propulsion load cases, where the engine torque and the gyroscopic loads of the two propellers are calculated at different engine operational points.

3.2 Loads Software and Quality Control

The DLR Institute of Aeroelasticity is a research organization and the methods and tools are designed for research applications. However, several steps are taken to ensure high quality and reliable results. In a first step, the loads process itself is certified according to DIN EN ISO 9001:2015 and described in a quality management handbook. In addition to that, the aeroelastic models are version controlled in a Mercurial repository. In that way, unintentional changes are difficult and all modifications are traceable. Because the gust loads analyses require a non-linear, closed-loop simulation of the free-flying aircraft in the time domain as explained in [6], standard software such as MSC.Nastran SOL146 is not applicable. Calculating the dynamic landing load cases would be difficult as well. Therefore, the Loads Kernel software is selected, developed by the first author [22]. The Loads Kernel software is version controlled in a Mercurial repository, including mechanisms for continuous quality control. For example, test cases that cover the core functionality are calculated in an automated way and compared to a reference after each commit. The software itself as well as the underlying aerodynamic panel methods are documented [8, 9] and publicly available.

Input to the aeroelastic models, such as mass and stiffness properties, are subject to a manual inspection for every sizing loop with respect to adequacy, plausibility and completeness. The output, such as dimensioning loads, models or results from aeroelastic analyses, are documented and accompanied by release notes. All documents are reviewed and cleared in an internal process.

3.3 Load Envelopes

The resulting nodal loads are integrated at so-called monitoring stations, for example along the wing, to create section loads. For the wing, interesting quantities are for example the shear force F_z , bending moment M_x or torsional moment M_y . For dynamic loads, time slices are used, allowing to merge for example

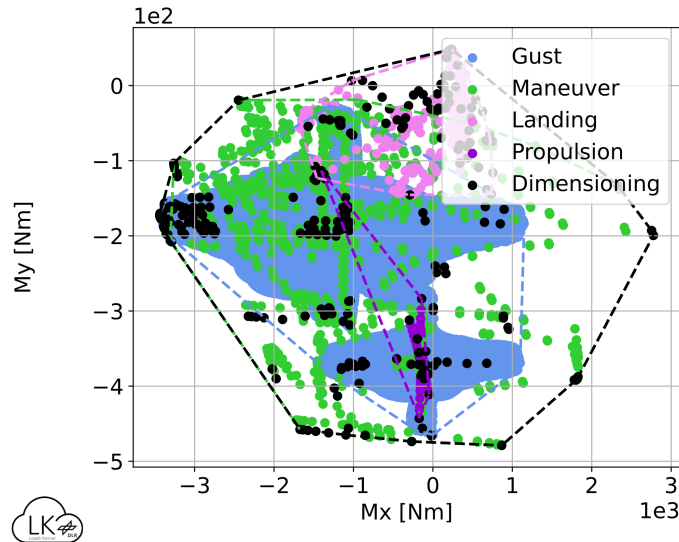


Figure 6: Identification of dimensioning load cases at the left wing root using load envelopes and the convex hull.

Table 3: Summary of load envelopes applied for the identification of dimensioning load cases.

| Component | F_z/M_x | M_x/M_y | F_y/M_x | M_x/M_z | M_y/M_z |
|-----------|-----------|-----------|-----------|-----------|-----------|
| Left Wing | x | x | | | |
| VTP | | | x | x | |
| Left HTP | x | x | | | |
| Fuselage | | x | | | x |
| Pylon | | x | | | x |

maneuver loads, which are calculated as trim cases, and gust loads. Because of the large number of load cases, a filtering needs to be applied. The dimensioning load cases are identified with two-dimensional load envelopes which show a combination of two interesting quantities / section loads. A summary of the load envelopes applied for the identification of dimensioning load cases is given in Table 3. Because the wing, the HTP and the VTP have no sweep, the section loads are calculated in the global coordinate system (x-y-z directions: aft-right-up) for all components. Also, because the aircraft is symmetrical, it is sufficient to evaluate and size only the left-hand side of the wing and the HTP as indicated in the table, leading to a total number of 132 load envelopes. In this way, ≈ 150 load cases are identified, which leads to ≈ 300 time-correlated sets of section loads because for example the same gust can cause peak loads at different sections at different time steps. An example for the torsional moment M_y and the bending moment M_x at the left wing root is given in Figure 6. First, one can see that the envelope has a rather round shape, which can be explained by the unswept wing, leading to no direct correlation between bending and torsional moments. Second, one can see that the highest negative bending moments M_x are reached by the gust loads while the highest negative torsional moments M_y are caused by maneuver loads. However, both maneuver and gust are very close to each other, which is an indicator for well-selected load cases which harmonize with each other in the sense that there are no extreme load cases which dominate the design. Third, it can be seen that the landing impact and the propulsion loads are within the envelope and/or of lower amplitude, which is as expected for the wing root. In the following, more detailed examples are given and discussed based on one-dimensional envelopes along the wing-span, which are easier to understand compared to a large number of two-dimensional load envelopes.

Figure 7 shows the envelope of the bending moment M_x along the wing span and each dot marks the highest positive or negative bending moment at one monitoring station. Comparing left- and right-hand side, the bending mo-

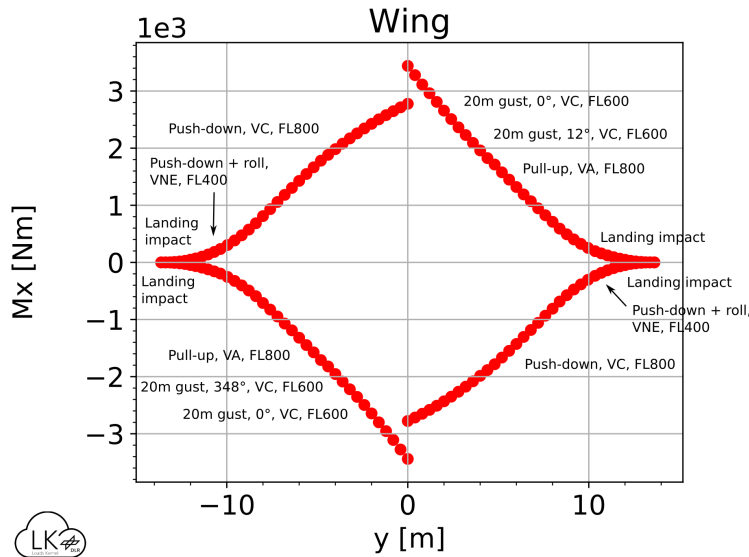


Figure 7: Bending moment M_x along the wing.

ments are symmetrical with swapped signs because the x-axis of the coordinate system points rearwards for both sides (global coordinate system). At the left inner wing, the largest negative bending moment is caused by the 0° (upward) gust at VC and FL600. Moving further outboard, the 348° gust at VC and FL600, which is orthogonal to the outer wing, causes largest negative bending moments, followed by the pull-up maneuver at VA and FL800. At the wing tip, both positive and negative bending moments are caused by the landing impact, which can be explained by the sudden (de-)accelerations of aircraft in vertical direction when the skid touches ground in combination with the structural dynamic reaction. The highest positive bending moments are due to the push-down maneuver at VC and FL800 for most parts of the inner and middle left wing, with a combined push-down and roll maneuver at VNE and FL400 showing up at a few monitoring stations at the outer wing. This can be explained by the nose-down wing torsion due to the $C_{m_{y,0}}$ of the airfoil, which is highest at VNE (max. q_∞), plus the additional nose-down torsion due to a downward aileron deflection, which causes negative lift at the outer wing.

The torsional moment M_y along the wing span is shown in Figure 8 and the corresponding load cases are more diverse compared to the bending moment M_x . The y-axis of the coordinate system points towards the right for both sides (global coordinate system), so that a negative sign indicates a nose-down torsional moment for both side, too. For most parts of the wing, the highest negative torsional moments M_y is due to a pull-up maneuver during roll combined with a roll acceleration in opposite direction (e.g. $+p, -\dot{p}$ and vice versa), which can be explained by considering three different effects. First, as already mentioned above, the $C_{m_{y,0}}$ of the cambered airfoil introduces a nose-down torsional moment, which is largest at VNE. Second, a downward aileron deflection leads to an additional torsional moment and third, the engine mass mounted on a pylon in front of the wing introduces a torsional moment if exposed to a vertical acceleration from both pull-up and accelerated roll. All three effects create torsional moments acting in the same direction. In the mid-wing area, the gyroscopic loads from the propeller show up, which create a torsional moment when the aircraft performs a yawing motion. In the outer wing area, several different load cases are identified, most of them just for a few monitoring stations. One of them is the landing impact, in this case not introduced by the main landing skid at the fuselage but by the landing skids located at the outer wing. As soon as the wing landing skids touch ground, the friction causes a negative torsional moment M_y . In addition, due to the positive dihedral of

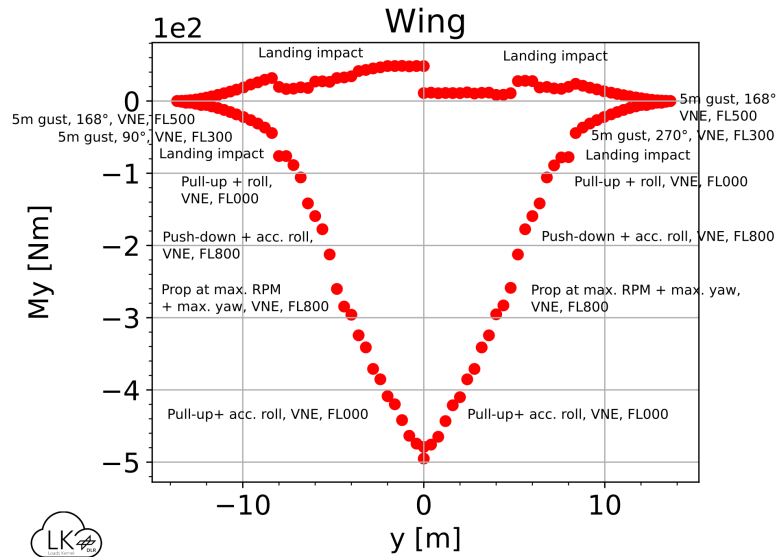


Figure 8: Torsional moment M_y along the wing.

the outer wing, the inertial forces of the out-of-plane masses create a torsional moment M_y acting in the same direction. The 90/270° (lateral) gust might be a little surprising at the outer wing, because its main effect could be expected at the VTP. However, the impact of the gust on the VTP combined with a reaction of the flight controller leads to a yawing motion. Because the gust gradient of only 5m indicates a very short gust, the yawing acceleration might be abrupt and, in combination with the structural dynamic behavior, trigger high acceleration at the outer wing and inertial forces of the out-of-plane masses. While the negative torsional moments M_y are symmetrical, this is not the case for the positive torsion moments M_y . However, the highest positive torsional moments are all caused by the landing impact, which excites an in-plane bending motion of the wing. As already explained above, this leads to a bending-torsion-coupling due to the out-of-plane masses. Because both the landing simulations and the structural dynamic properties are not perfectly symmetrical, the results are unsymmetrical as well. Although this is interesting from an academic perspective, the positive values are about one order of magnitude smaller than the negative values and not important for the structural sizing.

3.4 Structural Sizing

Based on the section loads presented above, the DLR Institute of Composite Structures and Adaptive Systems performs the structural sizing of the overall aircraft, which is an iterative process, since changes in the structure have an effect on the loads and vice versa.

An algorithm based on analytical methods is used for the sizing, verified by numerical models. A beam model (Bernoulli theory) and section loads are used to dimension the main structural elements, such as wing and tail spars and the longerons (fuselage, pylons). For the lifting surfaces, a carbon fiber tube is used as main spar, located at 25% chord length. The masses of other elements like ribs, wing covering including solar generator or joining elements are scaled volumetrically or two-dimensionally, which is sufficient on this level of aircraft design. Detailed Finite element models (DFEMs) are created to verify the design and mass estimation of particularly critical elements/areas (such as bonded connections, rib scaling, wing-fuselage-joint).

The sizing criteria of the beam elements are material strength, stability and torsional and bending stiffness demands. For instance, for the spars, the design parameters are tube thickness, tube diameter, rib or frame spacing and material parameters (laminate stacking). As material model, a smeared wound laminate

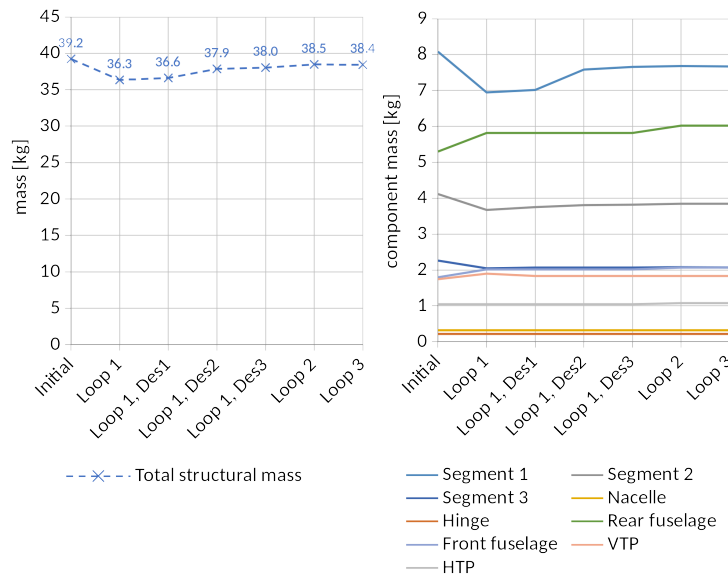


Figure 9: Convergence history of the structural masses.

is considered, so that thickness is the only design parameter for a given laminate with smeared stiffness and strength properties. Different laminate set-ups are studied for each design loop as design variations, which are also listed in Figure 9. A minimum material thickness prevents non-manufacturable wall thicknesses. For the very thin laminates the usage of smeared laminate properties has to be done with caution, not to overestimate the engineer constants. Knock-down factors are used to account for material and process scatter or thermal conditions when the test data does not cover the entire operating temperature range.

The iterative loads and structural sizing process typically starts with a loads analysis, followed by the structural sizing, and the loops are repeated until mass convergence is achieved. The initial loop is started with a simple analytical load distribution. The identification procedure for the dimensioning load cases typically results in ≈ 300 sets of time-correlated section loads as described in section 3.3 and all of them can be included for the sizing very time efficiently using the analytical model. This is advantageous because a high number of e.g. laminate stackings can be calculated for all load cases to obtain the lightest structure. Note that the section loads are computed as limit loads (LL), the structural sizing is performed based on ultimate loads ($UL = LL \cdot 1.5$). From all load cases, the heaviest configurations are summarized and returned to the next load calculation.

It can be seen that with the evolution of the HAP configuration, the iterative sizing process reaches mass convergence within 3-5 iterations, see Figure 9, which is determined by a change of mass $\leq \pm 100$ g. The wall thickness e.g. of the wing spar ranges between 0.4 mm at the outside and 1.6 mm at the wing root, see Figure 10.

4. Aeroelastic Analyses

4.1 Jig and Flight Shapes

Figure 11 shows an overview of the elastic deformations of the main wing for the horizontal level flight at selected flight speeds. It can be seen that the wing has a negative, nose-down elastic twist $U_{\text{flex},ry}$ for all flight conditions and the higher the flight speed, the stronger the twist, meaning that the lift is reduced towards the wing tip and shifted towards the inner wing with some negative lift at the wing tip for VNE. This has an influence on the wing bending $U_{\text{flex},z}$, which is highest for VS and slightly negative for VNE. Note that while the wing bends upwards, the fuselage shifts downwards, leading to a total deflection of ≈ 0.9 m

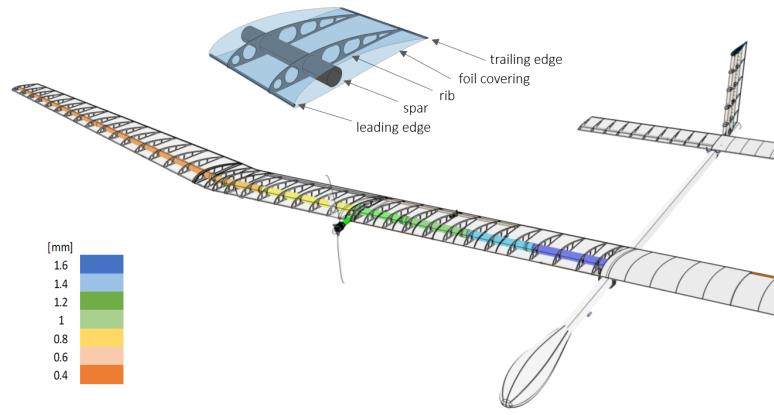


Figure 10: Distribution of the wall thickness of the wing spar.

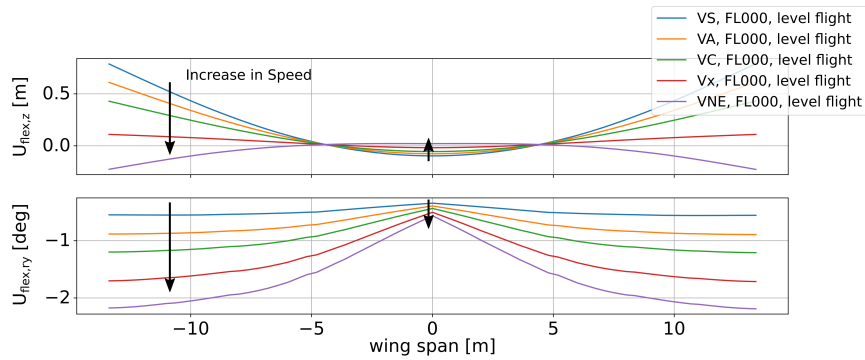


Figure 11: Elastic deformation of the main wing at selected flight speeds.

for horizontal level flight, which corresponds to $\approx 6.6\%$ of the half wing span. It can be concluded that the aircraft, with its slender and extreme light-weight construction, is highly elastic but the assumption of linear elasticity still holds true. Even for a pull-up maneuver, deflections of $\leq 15\%$ are calculated, thus geometrically nonlinear effects [23] are still small and negligible.

The elastic twist distribution $U_{flex,ry}$ is also the basis to determine the jig shape. Because a desired wing twist is given by the optimal lift distribution at VO_{min} , the jig shape is calculated such that jig shape + elastic deformation = flight shape. The results for the wing are given in Table 4 and include an angle of incidence of 3.50° w.r.t the fuselage. The adjustments can be achieved by mounting the ribs on the main tube at an angle interpolated from the table.

4.2 Control Surface Effectiveness

The non-dimensional stability and control derivative coefficients are calculated using the elastic coefficients of the unrestrained vehicle as obtained from the Loads Kernel [8]. The control surface effectiveness is calculated by dividing the elastic coefficients by the rigid coefficients. The resulting values are listed in Table 5. There is no aeroelastic control reversal at all operational points. High aileron effectiveness of 0.63 at VNE is achieved by using two long ailerons with a small depth in chord direction and by selecting an inboard location.

Table 4: Flight and jig shape for the left and right wing.

| y | Flight shape | Elastic deformation | Jig shape |
|----------|--------------|---------------------|--------------|
| 0.0 m | 5.00° | -0.41° | 5.41° |
| 8.0 m | 3.02° | -0.84° | 3.86° |
| 13.624 m | 2.60° | -0.89° | 3.49° |

| | Ailerons ξ ($C_{m,x}^{\text{flex}}/C_{m,x}^{\text{rigid}}$) | Elevator η ($C_{m,y}^{\text{flex}}/C_{m,y}^{\text{rigid}}$) | Rudder ζ ($C_{m,z}^{\text{flex}}/C_{m,z}^{\text{rigid}}$) |
|---------------------------------|--|---|--|
| VS (at sea level) | 0.94 | 0.99 | 0.95 |
| VA (at sea level) | 0.88 | 0.98 | 0.91 |
| VC | 0.81 | 0.97 | 0.88 |
| Vx | 0.72 | 0.96 | 0.82 |
| VNE | 0.63 | 0.95 | 0.77 |
| Super Dive ($1.15 \cdot VNE$) | 0.49 | 0.94 | 0.70 |

Table 5: Aeroelastic control surface effectiveness.

| | $AC_x[m]$ | $CG_x[\% \text{ MAC}]$ | $\alpha_{\text{trim}} [^\circ]$ | $\eta_{\text{trim}} [^\circ]$ |
|---------------------------------|-----------|------------------------|---------------------------------|-------------------------------|
| VS (at sea level) | 5.59 m | 35.0 % | 6.47° | -3.29° |
| VA (at sea level) | 5.61 m | 36.4 % | -0.27° | 1.23° |
| VC | 5.62 m | 37.1 % | -2.34° | 2.55° |
| Vx | 5.64 m | 38.6 % | -3.66° | 3.30° |
| VNE | 5.66 m | 40.0 % | -4.12° | 3.48° |
| Super Dive ($1.15 \cdot VNE$) | 5.68 m | 41.4 % | - | - |

Table 6: Aeroelastic shift of the aerodynamic center.

4.3 Longitudinal Stability

The x-location of the aerodynamic center AC_x is calculated with

$$AC_x = x_{\text{ref}} - \frac{c_{\text{ref}} \cdot dC_{my}/d\alpha}{dC_z/d\alpha} \quad (7)$$

using the elastic coefficients of the unrestrained vehicle as obtained from the Loads Kernel [8]. The resulting values are listed in Table 6. The AC_x of the elastic aircraft does not shift in front of the $CG_x = 5.1 \text{ m}$ at all operational points, which is also indicated in the third column by the CG_x given in % MAC. Instead, the AC_x even moves further rearwards with increasing dynamic pressure, which is contrary to typical transport type aircraft where the aerodynamic center shifts forwards, and can be explained partially by the unswept wing. In addition, the mass distribution and the fuselage bending characteristics introduce a downward deflection of the nose and a negative twist at the wing root that increases with flight speed, which could be seen from $U_{\text{flex,ry}}$ in Figure 11 already. In addition, in the last columns of Table 6, the angle of attack α and the elevator deflection η for a trimmed horizontal level flight is given, as requested by the reviewer.

4.4 Flutter Check

The flutter analyses is performed at selected operational conditions only, in this case at FL000, FL400 and FL800. Note that the flutter check does not replace a comprehensive flutter analysis, but is performed with the intention to reveal and avoid any obvious flutter mechanism already during the preliminary design. Both mass configuration M1 and M2 have been considered and show very similar results, thus only the results for M1 are presented for one operational point at flight level FL400 in Figure 12. A modal damping of 2% is assumed for all modes, which corresponds to a damping $d = -0.02$ in Figure 12. Note that the mode tracking algorithms showed some issues and there is still some jumping / mode switching visible in the plots. Also note that several modes show an aperiodic behavior, their frequency drops to zero with increasing speed while the damping approaches -1.0. This can be explained by the low wing stiffness and mass in comparison with e.g. the aerodynamic damping forces of the long, high aspect ratio wing. The results are calculated using a PK method following Hassig [24], implemented in the Loads Kernel software. For the application on the HAP configuration, the PK method has been modified in the following way to improve results:

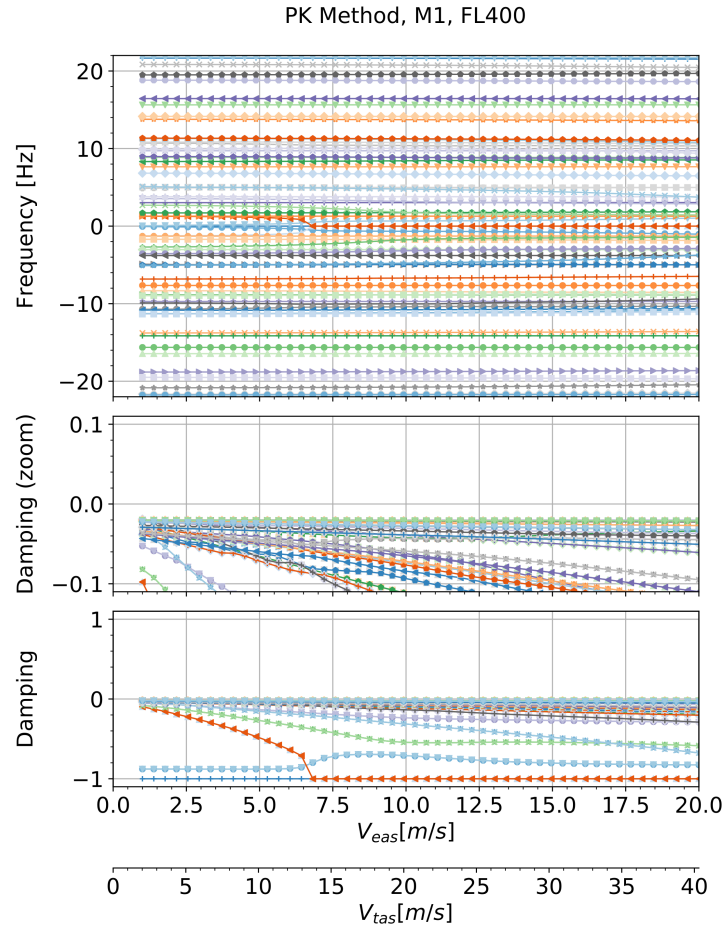


Figure 12: Flutter solution with modified PK method, M1, FL400.

- All complex eigenvalues are considered, not only those with a positive imaginary part, so that no eigenvalue can be “lost” due to a poor tracking, especially when approaching $f = 0.0 \text{ Hz}$. However, this means that all positive frequencies get a negative counterpart.
- The MSC.Nastran damping definition of $d = 2 \cdot \frac{\lambda^{Re}}{\lambda^{Im}}$ is replaced by $d = \frac{\lambda^{Re}}{|\lambda|}$ so that the resulting damping ranges between $d = 0.0 \dots \pm 1.0$.
- The mode tracking compares the eigenvector instead of the eigenvalues.
- A relaxation factor is introduced in the PK iteration loop to improve convergence.
- The generalized aerodynamic matrix \mathbf{Q}_{hh} is not divided by the reduced frequency k_{red} , thus the results for small k_{red} should be better and, theoretically, even $k_{red} = 0.0$ is possible.

The results have been cross-checked with MSC Nastran SOL145. Both solutions show no flutter and/or divergence at all operational points and up to $1.15 \cdot V_{NE} \approx 18.0 \text{ m/s}$.

4.5 Interaction of Flexible Modes with Flight Mechanics

To better investigate the influence of the low-frequency elastic modes on the oscillatory flight mechanical modes, a state space system is set up. The difference with respect to the PK flutter solution of the previous section is that only quasi-steady aerodynamics are employed, which is justified by the focus on the low-frequency range only, and avoids problems with poor convergence during the PK iteration loops. Note that Figure 12 from the previous section has the

intention to show elastic modes while this section focuses on the rigid body and low frequency elastic modes. The results are comparable, but not identical, and the symbols and colors have switched between this and the previous section. A simplified analysis with the first four elastic modes is discussed in the following. From Figure 13 it can be seen that the frequency of the short period mode slowly rises with speed and that the first wing bending frequency slowly drops until approaching each other at $V_{EAS} \approx 7 \text{ m/s}$. In addition, the eigenvalues and the modal participation are shown in Figure 14. The plot can be considered as a slice from Figure 13 for a speed of $V_{EAS} = 4.88 \text{ m/s}$ and the dashed lines indicate the trajectory of the eigenvalues. The eigenvalues 3 and 4 show for example the short period and eigenvalues 5 and 6 the first wing bending mode. Starting close to zero at low speed, the imaginary part of eigenvalues 3 and 4 (short period) rises but approaches zero again for higher speeds. Then the real part of eigenvalue 4 decreases (more damping) while the real part of eigenvalue 3 increases (less damping). Concerning stability, both eigenvalues need to be monitored, which is the motivation for the modified PK method described above. Looking at eigenvalues 5 and 6 (first wing bending) the imaginary part decreases with higher speed from $\approx 1.3 \text{ Hz}$ to $\approx 0.7 \text{ Hz}$, approaching the short period like observed before in Figure 13. The modal participation factors are given in the lower plot. On the x-axis the eigenvalues are given, the y-axis shows all states involved in the analysis. The state space system includes the rigid body velocities v , w and rates p , q and r , where the superscript ' denotes the FEM coordinates system, and the integrals y , z , Φ , Θ and Ψ . The states u and x are excluded for numerical reasons (no drag), therefore the phugoid mode is missing. The first four flexible mode shapes are labeled with U_f for the modal displacements and \dot{U}_f for the modal velocities. Looking at the modal participation of eigenvalues 3 and 4 (short period), which ranges from 0.0 to 1.0 and is indicated by the color, one can see that the rigid body velocity w with some contribution from the pitching velocity q is involved, which is as expected for a short period mode. However, there is also a strong contribution from the first and second flexible modes visible. Remember that as explained in section 2.3, the first out-of-plane and in-plane wing bending modes occur in combination.

A second coupling effect can be seen for eigenvalue 0, which represents the roll mode in combination with the first antisymmetric wing bending. From the modal participation factor it can be seen that the modal velocity of the fourth flexible mode actually has a much larger participation factor than the roll rate p .

A third coupling effect is observed for eigenvalues 1 and 2, which show the dutch-roll mode. From the modal participation it can be seen that mainly the states Ψ , v and r are involved but there is also a slight contribution from the modal displacement and velocity of mode 3, which is an antisymmetric fuselage bending. For this selected velocity, the coupling is rather weak, but it increases significantly for higher flight speeds.

5. Summary and Outlook

In this work, results from the loads and aeroelastic analyses of a high altitude, long endurance, solar electric aircraft have been presented. The simulations were based on a carefully selected aeroelastic modeling and adequate methodologies. The level of detail and maturity of the input data corresponds to a preliminary design level and, in fact, the data presented in this publication was used to pass a preliminary design review. The results of the analyses are plausible and confirm the selected design from an aeroelastic perspective. Some insights and details on selected flight-physical effects were given to the reader and discussed.

The next steps towards a critical design review will include an update of the system masses and a more detailed structural model. Especially the stiffness in chord direction, mainly from the ribs, is important to better evaluate the control

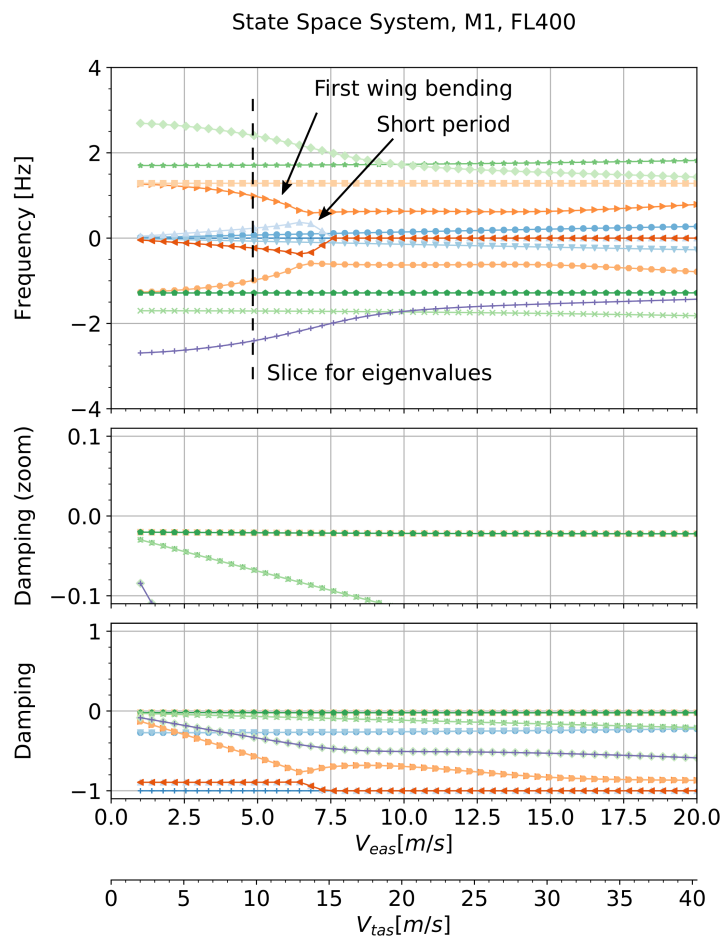


Figure 13: State space analysis, M1, FL400.

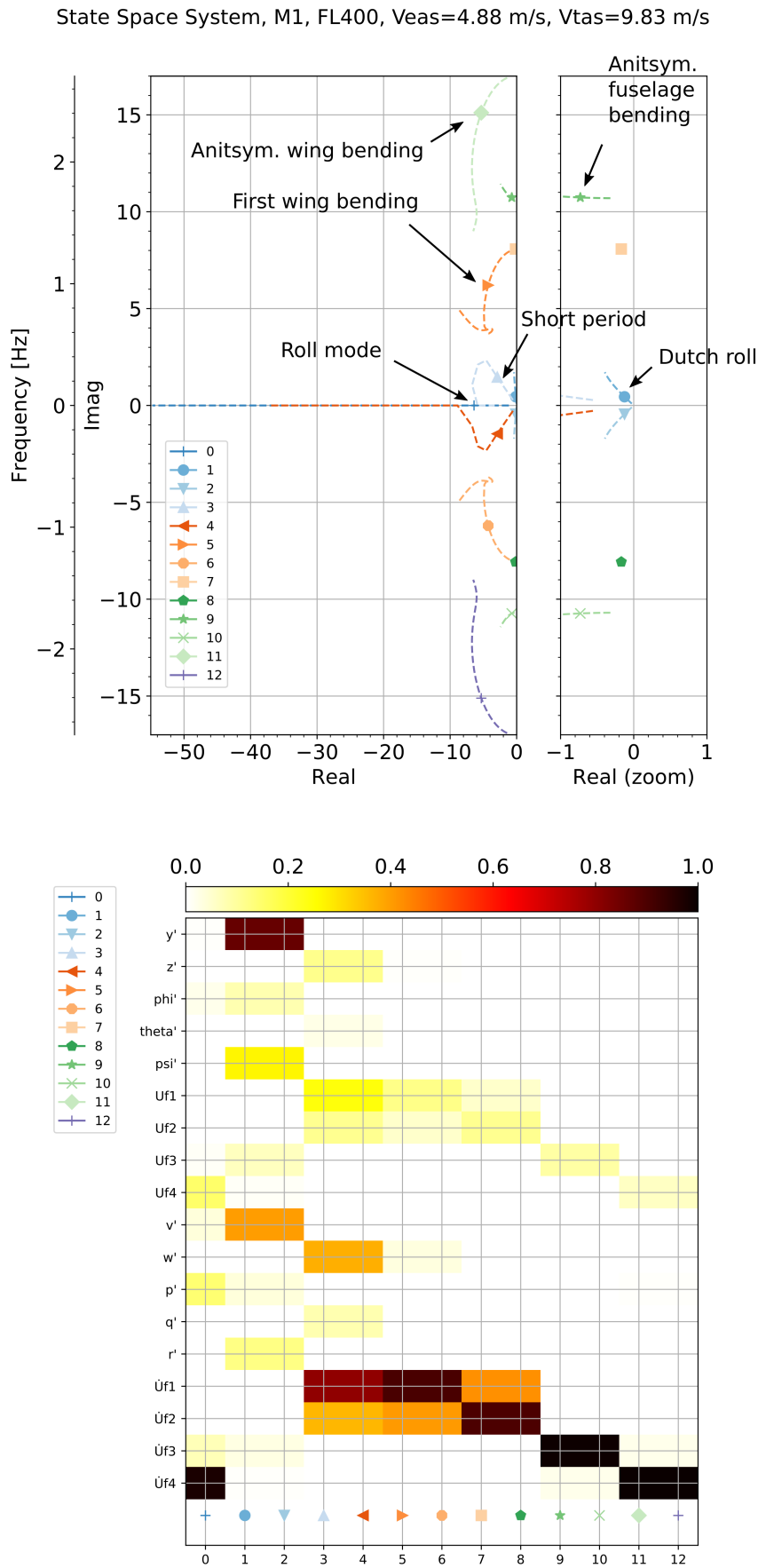


Figure 14: Eigenvalues and modal participation factors of the state space system, M1, FL400.

surfaces. Modeling of the attachments and actuator stiffness is important to assess control surface flutter, which will be part of a more comprehensive flutter analysis. The design load assumptions will be refined and/or confirmed with results from flight mechanical analyses and the flight controller will be updated accordingly. All these updates will then lead to a new structural sizing, however, the authors expect similar results and believe that the results shown in this work are representative for the final configuration.

To validate the simulation models, a number of test are planned. With respect to aeroelasticity, this is mainly the ground vibration test, which will be performed on the final aircraft to identify the structural dynamic properties experimentally. This allows to validate and, if necessary, update the finite elements model. For the flight test, both strain and acceleration measurements are planned. Based on the strain gages, load measurements are possible in an indirect way, which involves a calibration procedure on ground to establish the relation between loads and strains.

References

- [1] Luca Benassi and Carlo Aquilini. The Structural Dynamics of Flying Non Stop for 100 Days. In *18th International Forum on Aeroelasticity and Structural Dynamics*, Savannah, Georgia, June 2019.
- [2] QinetiQ. QinetiQ's Zephyr UAV exceeds official world record for longest duration unmanned flight, September 2007. <https://www.qinetiq.com/media/news/releases/Pages/qinetiqs-zephyr-exceeds-world-record.aspx>.
- [3] Karl Schwarz. Hochfliegendes UAV: BAE übernimmt PHASA-35-Entwicklung, September 2019. <https://www.flugrevue.de/militaer/hochfliegendes-uav-bae-uebernimmt-phas-a-35-entwicklung/>.
- [4] Solar Impulse SA. Solar Impulse - Around the world to promote clean technologies. <http://www.solarimpulse.com/>.
- [5] Yvonne Gibbs. NASA Armstrong Fact Sheet: Helios Prototype, August 2015. <http://www.nasa.gov/centers/armstrong/news/FactSheets/FS-068-DFRC.html>.
- [6] Arne Voß, Vega Handojo, Christian Weiser, and Steffen Niemann. Preparation of Loads and Aeroelastic Analyses of a High Altitude, Long Endurance, Solar Electric Aircraft. In *AEC2020 Aerospace Europe Conference*, Bordeaux, France, February 2020. CEAS and 3AF. <https://elib.dlr.de/133496/>.
- [7] Thomas Klimmek. Parameterization of topology and geometry for the multidisciplinary optimization of wing structures. In *CEAS 2009 - European Air and Space Conference*, Manchester, United Kingdom, October 2009. Council of European Aerospace Societies.
- [8] Arne Voß. Loads Kernel User Guide, Version 1.01. Technical Report DLR-IB-AE-GO-2020-136, Institut für Aeroelastik, Deutsches Zentrum für Luft- und Raumfahrt, Göttingen, Germany, November 2021. <https://elib.dlr.de/140268/>.
- [9] Arne Voß. An Implementation of the Vortex Lattice and the Doublet Lattice Method. Technical Report DLR-IB-AE-GO-2020-137, Institut für Aeroelastik, Deutsches Zentrum für Luft- und Raumfahrt, Göttingen, Germany, 2020. <https://elib.dlr.de/136536/>.

- [10] Martin R. Waszak and David K. Schmidt. Flight dynamics of aeroelastic vehicles. *Journal of Aircraft*, 25(6):563–571, June 1988. <http://arc.aiaa.org/doi/abs/10.2514/3.45623>.
- [11] Martin Waszak, Carey Buttrill, and David Schmidt. Modeling and Model Simplification of Aeroelastic Vehicles: An Overview. Technical Report NASA Technical Memorandum 107691, NASA Langley Research Center, September 1992.
- [12] Carey Buttrill, Thomas Zeiler, and P. Arbuckle. Nonlinear simulation of a flexible aircraft in maneuvering flight. In *Flight Simulation Technologies Conference, Guidance, Navigation, and Control and Co-located Conferences*. American Institute of Aeronautics and Astronautics, August 1987. <http://arc.aiaa.org/doi/10.2514/6.1987-2501>.
- [13] Yasim Hasan, Mathias Roeser, Steffen Niemann, Martin Hepperle, Arne Voß, Vega Handoyo, and Christian Weiser. Flight Mechanical Design and Analysis of a Solar-Powered High-Altitude Platform. In *Deutscher Luft- und Raumfahrtkongress*, Online Conference, 2020. Deutsche Gesellschaft für Luft- und Raumfahrt - Lilienthal-Oberth e.V.
- [14] Alexander Köthe. *Flight Mechanics and Flight Control for a Multibody Aircraft*. Dissertation, TU Berlin, Berlin, Germany, 2019. <https://doi.org/10.14279/depositonce-7555>.
- [15] Manuel Pusch, Daniel Ossmann, and Tamás Luspay. Structured Control Design for a Highly Flexible Flutter Demonstrator. *Aerospace*, 6(3):27, March 2019. <https://www.mdpi.com/2226-4310/6/3/27>.
- [16] A-6A3 Flight Control and Vehicle Management Systems Cmt. Aerospace - Vehicle Management Systems - Flight Control Design, Installation and Test of, Military Unmanned Aircraft, Specification Guide For. Technical Standard ARP94910, SAE International, December 2012. <https://www.sae.org/content/arp94910>.
- [17] A-6A3 Flight Control and Vehicle Management Systems Cmt. Vehicle Management Systems - Flight Control Function, Design, Installation and Test of Piloted Military Aircraft, General Specification For. Technical Standard AS94900A, SAE International, August 2018. <https://www.sae.org/content/as94900a>.
- [18] Christian Weiser and Daniel Ossmann. Baseline Flight Control System for High Altitude Long Endurance Aircraft. In *AIAA Scitech Forum*, 2022, accepted.
- [19] Daniel Ossmann, Tamas Luspay, and Balint Vanek. Baseline Flight Control System Design for an Unmanned Flutter Demonstrator. In *2019 IEEE Aerospace Conference*, pages 1–10, Big Sky, MT, USA, March 2019. IEEE. <https://ieeexplore.ieee.org/document/8741853/>.
- [20] Pierre Apkarian, Minh Ngoc Dao, and Dominikus Noll. Parametric Robust Structured Control Design. *IEEE Transactions on Automatic Control*, 60(7):1857–1869, July 2015. <http://ieeexplore.ieee.org/document/7027164/>.
- [21] European Aviation Safety Agency, editor. *Certification Specifications for Normal-Category Aeroplanes CS-23*. Amendment 3 edition, July 2012. <https://www.easa.europa.eu/certification-specifications/cs-23-normal-utility-aerobatic-and-commuter-aeroplanes>.

- [22] Arne Voß. *Design and Structural Optimization of a Flying Wing of Low Aspect Ratio Based on Flight Loads*. Dissertation, Technische Universität Berlin, Berlin, Germany, 2020. <http://dx.doi.org/10.14279/depositonce-9858>.
- [23] Markus Raimund Ritter. *An extended modal approach for nonlinear aeroelastic simulations of highly flexible aircraft structures*. Doctoral Thesis, TU Berlin, 2019. <https://depositonce.tu-berlin.de/handle/11303/9586>.
- [24] H. J. Hassig. An approximate true damping solution of the flutter equation by determinant iteration. *Journal of Aircraft*, 8(11):885–889, November 1971.